Computer Physics Communications 216 (2017) 84–94

Contents lists available at ScienceDirect

Computer Physics Communications

journal homepage: www.elsevier.com/locate/cpc

# Phase-field simulations of crystal growth in a two-dimensional cavity flow

Seunggyu Lee [a], Yibao Li [b], Jaemin Shin [c], Junseok Kim [d,*]

[a] National Institute for Mathematical Sciences, Daejeon 34047, Republic of Korea
[b] School of Mathematics and Statistics, Xi'an Jiaotong University, Xi'an 710049, China
[c] Institute of Mathematical Sciences, Ewha W. University, Seoul 120-750, Republic of Korea
[d] Department of Mathematics, Korea University, Seoul 136-713, Republic of Korea

ARTICLE INFO

*Article history:*
Received 14 December 2015
Received in revised form 9 March 2017
Accepted 10 March 2017
Available online 20 March 2017

*Keywords:*
Crystal growth
Phase-field method
Moving overset grid
Cavity flow

ABSTRACT

In this paper, we consider a phase-field model for dendritic growth in a two-dimensional cavity flow and propose a computationally efficient numerical method for solving the model. The crystal is fixed in the space and cannot be convected in most of the previous studies, instead the supercooled melt flows around the crystal, which is hard to be realized in the real world experimental setting. Applying advection to the crystal equation, we have problems such as deformation of crystal shape and ambiguity of the crystal orientation for the anisotropy. To resolve these difficulties, we present a phase-field method by using a moving overset grid for the dendritic growth in a cavity flow. Numerical results show that the proposed method can predict the crystal growth under flow.



## 1. Introduction

Convection of the crystal in the melt is of great interest for the practical processes to understand the dendritic solidification. The formation of the solidification such as the arm spacing, growth rate, and morphology is largely changed by the forced convection due to the melt flow. The convective effects on free dendritic crystal growth have been investigated experimentally [1–5] and numerically [6–12]. In numerical investigation, the phase-field method, which has been widely applied to model various mesoscale phenomena such as solidification, recrystallization, and many energy-based applications [13–16], is also a flexible mathematical tool to describe the interfaces in dendritic crystal growth with convection. Two- and three-dimensional adaptive phase-field simulations of dendritic crystal growth in a forced flow were presented in [17]. The effect of natural convection in 3D dendritic growth using an efficient adaptive phase-field simulation was investigated by Chen and Lan [18]. A two-dimensional lattice Boltzmann method-cellular automation model was presented to investigate the dendritic growth of binary alloys in the presence of natural convection [19]. Recently, motion and growth of a dendrite in the presence of melt convection was modeled using a phase-field-lattice Boltzmann method [7].

However, the crystal is fixed in the space and cannot be convected, instead the supercooled melt flows around the crystal, which is hard to be realized in the real world experimental setting in the previous studies. Direct application of the advection term to the crystal equation would lead some problems such as the shape deformation and the ambiguity of the crystal orientation for the anisotropy. In recent years, few models have been elaborated for using two computational domains to distinguish between the fluid flow and the phase separation by applying a fictitious domain method [20], a combination of the volume of fluid and the immersed boundary methods [21]. Nevertheless, there are drawbacks in their algorithms; difficulty in matching the grids or computational efficiency. Note that the efficiency of the computational point of view is one of the most important issues in solid mechanics because of tackling massively large scale computational problem from implementation [22]. Therefore, the parallel computing is an active field in modeling evolution of dendrite microstructure [23–25].

The main purpose of the present paper is to resolve these difficulties by using a moving overset grid. The fluid domain is covered with a fixed Cartesian grid, while a moving overset grid is used to represent the crystal growth. The motion of the crystal is derived by calculating the translational and rotational force of the crystal phase. Using the fictitious domain method with distributed Lagrange multiplier method, the method in [20] has an advantage that simulations can be performed in a problem involving different scales in time and space. Note that the proposed method would be compared with the method in [20] since our moving overset grid method is similar to their method based on a fictitious domain method. However, our method is simpler to implement and it

* Corresponding author. Fax: +82 2 929 8562.
*E-mail address:* cfdkim@korea.ac.kr (J. Kim).
*URL:* http://math.korea.ac.kr/~cfdkim (J. Kim).

http://dx.doi.org/10.1016/j.cpc.2017.03.005
0010-4655/

also has the advantage involving different scales. As mentioned above, a large scale computational problem is an important issue in modeling dendritic growth and the parallel computing technique is actively studied. Therefore, the simpler algorithm can be contributed to parallelize or develop other kinds of computational methodologies.

This paper is organized as follows: the governing equations are described in Section 2. In Section 3, the computationally efficient operator splitting algorithm is discussed. The numerical results are presented for solving the crystal growth simulations under a cavity flow in Section 4. Finally, conclusions are given in Section 6. Note that this work is based on the Ph.D. thesis [26] of the first author, Korea University.

## 2. Mathematical modeling

We consider the solidification of a pure substance from its supercooled melt in a two-dimensional cavity flow. To model the solidification system, let $\phi(x, y, t)$ be the phase-field function, where $\phi = 1$ and $\phi = -1$ refer to the bulk solid and melt phases, respectively. The phase-field variable $\phi$ is smoothly changed but has small thickness across the interfacial transition region, and we define the interface by the zero level set of $\phi$ [12]. The governing equations for crystal growth in the flow are given as

$$\frac{\partial \mathbf{u}}{\partial t} + \mathbf{u}\cdot\nabla\mathbf{u} = -\nabla p + \frac{1}{Re}\nabla\cdot[\eta(\phi)(\nabla\mathbf{u} + \nabla\mathbf{u}^T)], \tag{1}$$

$$\nabla\cdot\mathbf{u} = 0, \tag{2}$$

$$\begin{aligned}\epsilon^2(\phi)\left(\frac{\partial\phi}{\partial t} + \mathbf{u}\cdot\nabla\phi\right) &= \nabla\cdot(\epsilon^2(\phi)\nabla\phi) + [\phi - \lambda U(1-\phi^2)](1-\phi^2)\\ &\quad + \left(|\nabla\phi|^2\epsilon(\phi)\frac{\partial\epsilon(\phi)}{\partial\phi_x}\right)_x + \left(|\nabla\phi|^2\epsilon(\phi)\frac{\partial\epsilon(\phi)}{\partial\phi_y}\right)_y,\end{aligned} \tag{3}$$

$$\frac{\partial U}{\partial t} + \mathbf{u}\cdot\nabla U = D\Delta U + \frac{1}{2}\frac{\partial\phi}{\partial t}, \tag{4}$$

where $\mathbf{u}$ is the velocity, $p$ is the pressure, $\eta(\phi)$ is the variable viscosity, and $U$ is the temperature. Note that Eqs. (1) and (2) are the Navier–Stokes equations [27] and Eqs. (3) and (4) are the governing equations for dendrite growth [28]. Here, $\eta(\phi) = 0.5[\eta_s(1+\phi) + \eta_m(1-\phi)]$, where $\eta_s$ and $\eta_m$ are viscosities of solid and melt, respectively. We take the increased viscosity approach [29] which uses a very large viscosity in the solid to describe the resistance to the flow. The dimensionless parameters are the Reynolds number $Re$, $\lambda$, and $D$. For the four-fold symmetry, $\epsilon(\phi)$ is defined as:

$$\epsilon(\phi) = (1-3\epsilon_4)\left(1 + \frac{4\epsilon_4}{1-3\epsilon_4}\frac{\phi_x^4 + \phi_y^4}{|\nabla\phi|^4}\right),$$

where $\epsilon_4$ is a parameter for the anisotropy of interfacial energy.

We will consider the two computational domains to separately represent the crystal growth and fluid flow. The flow with appropriate boundary conditions is defined on the base domain. The phase-field function $\phi$ for representing the crystal is defined on the relatively small domain, and the crystal growth equation is

$$\begin{aligned}\epsilon^2(\phi)\frac{\partial\phi}{\partial t} &= \nabla\cdot(\epsilon^2(\phi)\nabla\phi) + [\phi - \lambda U(1-\phi^2)](1-\phi^2)\\ &\quad + \left(|\nabla\phi|^2\epsilon(\phi)\frac{\partial\epsilon(\phi)}{\partial\phi_x}\right)_x + \left(|\nabla\phi|^2\epsilon(\phi)\frac{\partial\epsilon(\phi)}{\partial\phi_y}\right)_y\end{aligned} \tag{5}$$

by using Eq. (3) without the advection term $\mathbf{u}\cdot\nabla\phi$. For translating and rotating of the crystal domain, we use the conservation law of the linear and angular momentums. Since the crystal is governed

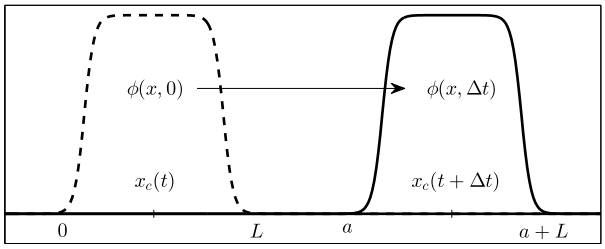


**Fig. 1.** Schematic of an advection for $\phi(x, t)$.

by a rigid body motion, the conservation of the linear momentum is given as:

$$M_c\mathbf{u}_c = \int_\Omega \mathbf{u}(x,y)\rho(x,y)\,d\mathbf{x}, \tag{6}$$

where $M_c$ is the total mass of a crystal, $M_c = \int_\Omega \rho(x,y)\,d\mathbf{x}$, $\Omega$ is a crystal, and $\mathbf{u}_c$ is the velocity of the crystal. If $\rho$ is constant, then we can rewrite Eq. (6) as

$$\mathbf{u}_c = \frac{\int_\Omega \mathbf{u}(x,y)\,d\mathbf{x}}{\int_\Omega d\mathbf{x}}. \tag{7}$$

We consider the advection equation to validate the motion by the linear momentum. For a rigid body motion, the motion of an advection can be represented by $\mathbf{x}_c(t+\Delta t) = \mathbf{x}_c(t) + \mathbf{u}_c\Delta t$ where $\mathbf{x}_c(t) = (x_c(t), y_c(t))$ is the center of mass. Here, a one-dimensional space is considered for simplicity (see Fig. 1).

On the other hand, the motion in Fig. 1 satisfies

$$\int_0^x \phi(\xi, 0)d\xi = \int_a^{x+a} \phi(\xi, \Delta t)d\xi.$$

By differentiating both sides, we get $\phi(x, 0) = \phi(x + a, \Delta t)$. Here, we can assume the constant velocity in the rigid body, i.e., $a = u\Delta t$. Since $\phi(x + a, \Delta t) = \phi(x, \Delta t) + u\Delta t\phi_x(x, \Delta t) + O(\Delta t^2)$ by the Taylor's expansion,

$$\frac{\phi(x, \Delta t) - \phi(x, 0)}{\Delta t} + u\phi_x(x, \Delta t) = 0,$$

which is approximated by the classical advection equation $\phi_t + u\nabla\phi = 0$ for a small $\Delta t$. From our derivation, the rigid body motion can be modeled by the classical advection equation only when a velocity field is a constant in the rigid body. To resolve this restriction, we propose the moving overset grid method which does not require a constant velocity field in the rigid body.

Next, the angular momentum $\mathbf{L}_c$ of the crystal is generally defined as a sum of the infinitesimal angular momentum $d\mathbf{L}$ [30]:

$$\mathbf{L}_c = \int_\Omega d\mathbf{L} = \int_\Omega \left(\tilde{\mathbf{r}}(x,y)\times\mathbf{u}(x,y)\right)\rho(x,y)\,d\mathbf{x}, \tag{8}$$

where $\tilde{\mathbf{r}}(x, y)$ is the displacement vector from the center of mass. Moreover, $\mathbf{L}_c$ can be written by a product of the moment of inertia $I_c$ and the angular speed $\omega_c$, i.e., $\mathbf{L}_c = I_c\omega_c$. Assuming the constant density $\rho = 1$, we have

$$\omega_c = \frac{\mathbf{L}_c}{I_c} = \frac{\int_\Omega(\tilde{\mathbf{r}}\times\mathbf{u})d\mathbf{x}}{\int_\Omega \|\,\tilde{\mathbf{r}}\,\|^2 d\mathbf{x}}. \tag{9}$$

Moreover, a rotation velocity of a rigid body can be treated as

$$\mathbf{u}(x,y) = \vec{\omega}\times\tilde{\mathbf{r}}(x,y).$$

The rotation can be approximated by the following equation:

$$\begin{bmatrix}x_c(t+\Delta t)\\ y_c(t+\Delta t)\end{bmatrix} = \begin{bmatrix}x_c(t)\\ y_c(t)\end{bmatrix} + \Delta t(\vec{\omega}\times\tilde{\mathbf{r}}). \tag{10}$$

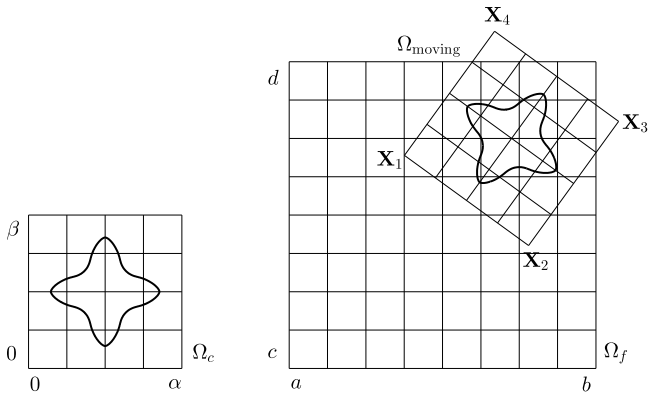


**Fig. 2.** Schematic illustration of the fluid domain $\Omega_f$, the crystal domain $\Omega_c$, and the moving domain $\Omega_{\text{moving}}$.

Note that $\overrightarrow{\omega} = (0, 0, \|\omega_c\|)$ and $\overrightarrow{\omega} \times \tilde{\mathbf{r}} = (-r_x\|\omega_c\|, r_y\|\omega_c\|, 0)$ in a two-dimensional domain where $\|\omega_c\|$ is the norm of $\omega_c$ and $\mathbf{r} = (r_x, r_y, 0)$. Since $\|\omega_c\| = \Delta\theta_c/\Delta t$ where $\Delta\theta_c$ is the rotational angle, Eq. (10) can be written as

$$\begin{bmatrix} \Delta x_c \\ \Delta y_c \end{bmatrix} = \Delta\theta_c \begin{bmatrix} -r_y \\ r_x \end{bmatrix}.$$

It is well-matched to the following rotation equation:

$$\begin{aligned} \begin{bmatrix} \Delta x_c \\ \Delta y_c \end{bmatrix} &= \begin{bmatrix} \cos(\Delta\theta_c) & -\sin(\Delta\theta_c) \\ \sin(\Delta\theta_c) & \cos(\Delta\theta_c) \end{bmatrix} \begin{bmatrix} r_x \\ r_y \end{bmatrix} - \begin{bmatrix} r_x \\ r_y \end{bmatrix} \\ &\approx \begin{bmatrix} 1 & -\Delta\theta_c \\ \Delta\theta_c & 1 \end{bmatrix} \begin{bmatrix} r_x \\ r_y \end{bmatrix} - \begin{bmatrix} r_x \\ r_y \end{bmatrix} = \Delta\theta_c \begin{bmatrix} -r_y \\ r_x \end{bmatrix}, \end{aligned}$$

for a small $\Delta\theta_c$. Therefore, we can translate and rotate a crystal without solving the advection term since the velocity vector and the angular speed of a crystal (or an overset grid) can be derived from Eqs. (7) and (9).

## 3. Numerical solution

In this section, we propose a hybrid numerical method using an overset grid for the simulation of the crystal growth in a cavity flow. Let $\Omega_f = (a, b) \times (c, d)$ be a domain for the fluid velocity $\mathbf{u} = (u, v)$, pressure $p$, and temperature $U$ with proper boundary conditions. Also, let $\Omega_c = (0, \alpha) \times (0, \beta)$ be another domain for the phase-field function $\phi$ with interpolated boundary conditions. $\Omega_{\text{moving}}$ is the coordinate transformation of $\Omega_c$, and it represents the location and rotation of $\Omega_c$ on $\Omega_f$. Let $\mathbf{X}_1, \mathbf{X}_2, \mathbf{X}_3, \mathbf{X}_4$ be corners of $\Omega_{\text{moving}}$ on $\Omega_f$ corresponding to points $(0, 0)$, $(\alpha, 0)$, $(\alpha, \beta)$, $(0, \beta)$ on $\Omega_c$, respectively. We determine the location of $\Omega_{\text{moving}}$ by setting its center as $\mathbf{m}_c = (\mathbf{X}_1+\mathbf{X}_2+\mathbf{X}_3+\mathbf{X}_4)/4$ and the rotation $\theta_c$ as the signed angle measured from the horizontal axis to the vector $\overrightarrow{\mathbf{X}_1\mathbf{X}_2}$ (see Fig. 2).

For the time integration, we consider the uniform time step $\Delta t = T/N_t$, where $T$ is the final time and $N_t$ is the total number of iterations. For $\Omega_f$, we use a uniform mesh with mesh spacing $h = (b - a)/N_x = (d - c)/N_y$, where $N_x$ and $N_y$ are the numbers of cells in the $x$- and $y$-directions, respectively. The center of each cell is located at $\mathbf{x}_{ij} = (x_i, y_j) = (a + (i - 0.5)h, c + (j - 0.5)h)$ and we define the computational domain $\Omega_f^h = \{\mathbf{x}_{ij} \mid i = 1, \ldots, N_x, j = 1, \ldots, N_y\}$. Using the marker-and-cell mesh, the pressure $p$ and temperature $U$ are defined at the cell centers and the velocities $u$ and $v$ are defined at the cell edges (see Fig. 3). Let $p_{ij}^n$ and $U_{ij}^n$ be approximations of $p(x_i, y_j, n\Delta t)$ and $U(x_i, y_j, n\Delta t)$, respectively. Let $u_{i+1/2,j}^n$ and $v_{i,j+1/2}^n$ be approximations of $u(x_i + h/2, y_j, n\Delta t)$ and $v(x_i, y_j + h/2, n\Delta t)$, respectively.

For $\Omega_c$, we also use a uniform mesh with mesh spacing $\bar{h} = \alpha/M_x = \beta/M_y$, where $M_x$ and $M_y$ are the numbers of cells in the $x$- and $y$-directions, respectively. The center of each cell is located at $\mathbf{s}_{kl} = (s_k^x, s_l^y) = ((k - 0.5)\bar{h}, (l - 0.5)\bar{h})$, and we define the computational domain $\Omega_c^h = \{\mathbf{s}_{kl} \mid k = 1, \ldots, M_x, l = 1, \ldots, M_y\}$. And, $\mathbf{m}_c^n$ and $\theta_c^n$ represent the center position and rotation of $\Omega_{\text{moving}}$ at time $n\Delta t$, respectively.

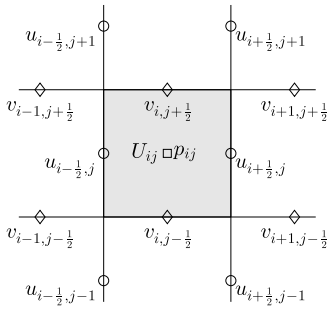


**Fig. 3.** Schematic of the computational grid for the pressure, velocities, and temperature.

Next, we describe our proposed numerical solution algorithm. At the $n$th time step, we have a divergence-free velocity field $\mathbf{u}^n$, the phase-field $\phi^n$, and temperature $U^n$. We seek $\mathbf{u}^{n+1}$, $p^{n+1}$, $\phi^{n+1}$, and $U^{n+1}$.

### 3.1. Hydrodynamic flow on $\Omega_f$

First, we solve Eqs. (1) and (2) to update $\mathbf{u}^{n+1}$ and $p^{n+1}$ on the fluid domain $\Omega_f$ by using the Chorin's projection method [31,32]:

$$\begin{aligned} \frac{\mathbf{u}^{n+1} - \mathbf{u}^n}{\Delta t} + \mathbf{u}^n \cdot \nabla_d \mathbf{u}^n &= -\nabla_d p^{n+1} \\ &\quad + \frac{1}{Re}\nabla_d \cdot \left[\eta^n \left(\nabla_d \mathbf{u}^n + (\nabla_d \mathbf{u}^n)^T\right)\right], \end{aligned} \tag{11}$$

$$\nabla_d \cdot \mathbf{u}^{n+1} = 0. \tag{12}$$

We solve an intermediate velocity field, $\tilde{\mathbf{u}}^n = (\tilde{u}^n, \tilde{v}^n)$:

$$\begin{aligned} \tilde{u}_{i+\frac{1}{2},j}^n &= u_{i+\frac{1}{2},j}^n - \Delta t(uu_x + vu_y)_{i+\frac{1}{2},j}^n \\ &\quad + \frac{\Delta t}{Re}\left(2(\eta u_x)_x + (\eta u_y)_y + (\eta v_x)_y\right)_{i+\frac{1}{2},j}^n, \end{aligned} \tag{13}$$

$$\begin{aligned} \tilde{v}_{i,j+\frac{1}{2}}^n &= v_{i,j+\frac{1}{2}}^n - \Delta t(uv_x + vv_y)_{i,j+\frac{1}{2}}^n \\ &\quad + \frac{\Delta t}{Re}\left((\eta v_x)_x + (\eta u_y)_x + 2(\eta v_y)_y\right)_{i,j+\frac{1}{2}}^n. \end{aligned} \tag{14}$$

The advection terms are defined by

$$(uu_x + vu_y)_{i+\frac{1}{2},j}^n = u_{i+\frac{1}{2},j}^n \bar{u}_{x_{i+\frac{1}{2},j}}^n + v_{i+\frac{1}{2},j}^n \bar{u}_{y_{i+\frac{1}{2},j}}^n, \tag{15}$$

$$(uv_x + vv_y)_{i,j+\frac{1}{2}}^n = v_{i,j+\frac{1}{2}}^n \bar{v}_{y_{i,j+\frac{1}{2}}}^n + u_{i,j+\frac{1}{2}}^n \bar{v}_{x_{i,j+\frac{1}{2}}}^n, \tag{16}$$

where the values $\bar{u}_{x_{i+\frac{1}{2},j}}^n$ and $\bar{u}_{y_{i+\frac{1}{2},j}}^n$ are computed using the upwind procedure

$$\bar{u}_{x_{i+\frac{1}{2},j}}^n = \begin{cases} \dfrac{u_{i+\frac{1}{2},j}^n - u_{i-\frac{1}{2},j}^n}{h}, & \text{if } u_{i+\frac{1}{2},j}^n > 0, \\ \dfrac{u_{i+\frac{3}{2},j}^n - u_{i+\frac{1}{2},j}^n}{h}, & \text{otherwise,} \end{cases} \tag{17}$$

$$\bar{u}_{y_{i+\frac{1}{2},j}}^n = \begin{cases} \dfrac{u_{i+\frac{1}{2},j}^n - u_{i+\frac{1}{2},j-1}^n}{h}, & \text{if } v_{i+\frac{1}{2},j}^n > 0, \\ \dfrac{u_{i+\frac{1}{2},j+1}^n - u_{i+\frac{1}{2},j}^n}{h}, & \text{otherwise.} \end{cases} \tag{18}$$

The quantities $\bar{v}^n_{x_{i,j+\frac{1}{2}}}$ and $\bar{v}^n_{y_{i,j+\frac{1}{2}}}$ are similarly computed. The viscosity terms are defined by

$$\begin{aligned}
&\left(2(\eta u_x)_x + (\eta u_y)_y + (\eta v_x)_y\right)^n_{i+\frac{1}{2},j} \\
&= 2\left(\eta^n_{i+1,j}\frac{u^n_{i+\frac{3}{2},j} - u^n_{i+\frac{1}{2},j}}{h^2} - \eta^n_{ij}\frac{u^n_{i+\frac{1}{2},j} - u^n_{i-\frac{1}{2},j}}{h^2}\right) \\
&\quad + \eta^n_{i+\frac{1}{2},j+\frac{1}{2}}\frac{u^n_{i+\frac{1}{2},j+1} - u^n_{i+\frac{1}{2},j}}{h^2} - \eta^n_{i+\frac{1}{2},j-\frac{1}{2}}\frac{u^n_{i+\frac{1}{2},j} - u^n_{i+\frac{1}{2},j-1}}{h^2} \\
&\quad + \eta^n_{i+\frac{1}{2},j+\frac{1}{2}}\frac{v^n_{i+1,j+\frac{1}{2}} - v^n_{i,j+\frac{1}{2}}}{h^2} \\
&\quad - \eta^n_{i+\frac{1}{2},j-\frac{1}{2}}\frac{v^n_{i+1,j-\frac{1}{2}} - v^n_{i,j-\frac{1}{2}}}{h^2}, \qquad (19)
\end{aligned}$$

$$\begin{aligned}
&\left((\eta v_x)_x + (\eta u_y)_x + 2(\eta v_y)_y\right)^n_{i,j+\frac{1}{2}} \\
&= \eta^n_{i+\frac{1}{2},j+\frac{1}{2}}\frac{v^n_{i+1,j+\frac{1}{2}} - v^n_{i,j+\frac{1}{2}}}{h^2} - \eta^n_{i-\frac{1}{2},j+\frac{1}{2}}\frac{v^n_{i,j+\frac{1}{2}} - v^n_{i-1,j+\frac{1}{2}}}{h^2} \\
&\quad + \eta^n_{i+\frac{1}{2},j+\frac{1}{2}}\frac{u^n_{i+\frac{1}{2},j+1} - u^n_{i+\frac{1}{2},j}}{h^2} - \eta^n_{i-\frac{1}{2},j+\frac{1}{2}}\frac{u^n_{i-\frac{1}{2},j+1} - u^n_{i-\frac{1}{2},j}}{h^2} \\
&\quad + 2\left(\eta^n_{i,j+1}\frac{v^n_{i,j+\frac{3}{2}} - v^n_{i,j+\frac{1}{2}}}{h^2} - \eta^n_{ij}\frac{v^n_{i,j+\frac{1}{2}} - v^n_{i,j-\frac{1}{2}}}{h^2}\right). \qquad (20)
\end{aligned}$$

Because the viscosity $\eta^n$ on $\Omega_f$ depends on the phase-field function $\phi^n$ on $\Omega_c$, we consider the interpolated function $\tilde{\phi}^n$ as follows: First, to check whether $\mathbf{x}_{ij} \in \Omega^h_f$ is inside of $\Omega_{\text{moving}}$ or not, we compare the sum of areas of four triangles with the area of moving domain $\Omega_{\text{moving}}$. That is, if

$$\begin{aligned}
&\triangle\mathbf{x}_{ij}\mathbf{X}_1\mathbf{X}_2 + \triangle\mathbf{x}_{ij}\mathbf{X}_2\mathbf{X}_3 + \triangle\mathbf{x}_{ij}\mathbf{X}_3\mathbf{X}_4 + \triangle\mathbf{x}_{ij}\mathbf{X}_4\mathbf{X}_1 \\
&\quad > \square\mathbf{X}_1\mathbf{X}_2\mathbf{X}_3\mathbf{X}_4, \qquad (21)
\end{aligned}$$

then it means that $\mathbf{x}_{ij} \notin \Omega_{\text{moving}}$ (Fig. 4(a)). If the two areas are same, then $\mathbf{x}_{ij} \in \Omega_{\text{moving}}$ (Fig. 4(b)). Next, we estimate the value of $\tilde{\phi}^n_{ij}$ from $\phi^n$ on $\Omega_c$ if $\mathbf{x}_{ij} \in \Omega_{\text{moving}}$ by using the bilinear interpolation and we define $\tilde{\phi}^n_{ij} = 1$ otherwise. For more details, we denote the directional vectors as $\mathbf{a} = \overrightarrow{\mathbf{X}_1\mathbf{X}_2}$, $\mathbf{b} = \overrightarrow{\mathbf{X}_1\mathbf{X}_4}$, and $\mathbf{c} = \overrightarrow{\mathbf{X}_1\mathbf{x}_{ij}}$. If $\mathbf{x}_{ij} \in \Omega_{\text{moving}}$, $\mathbf{x}_{ij}$ is corresponding to the location $((\mathbf{a}\cdot\mathbf{c})/|\mathbf{a}|, (\mathbf{b}\cdot\mathbf{c})/|\mathbf{b}|)$ on $\Omega_c$ and then we can calculate the $\tilde{\phi}_{ij}$ by the interpolation. Finally, we define

$$\eta^n_{ij} = \frac{\eta_s(1+\tilde{\phi}^n_{ij}) + \eta_m(1-\tilde{\phi}^n_{ij})}{2}. \qquad (22)$$

We then solve the pressure field at the $(n+1)$th time step.

$$\frac{\mathbf{u}^{n+1} - \tilde{\mathbf{u}}^n}{\Delta t} = -\nabla_d p^{n+1}, \qquad (23)$$

$$\nabla_d \cdot \mathbf{u}^{n+1} = 0. \qquad (24)$$

Applying the discrete divergence $\nabla_d\cdot$ and divergence-free Eq. (24) to Eq. (23), we obtain the Poisson's equation with the homogeneous Neumann boundary condition:

$$\Delta_d p^{n+1} = \frac{1}{\Delta t}\nabla_d \cdot \tilde{\mathbf{u}}^n, \qquad (25)$$

where $\Delta_d p^{n+1}_{ij} = (p^{n+1}_{i+1,j} + p^{n+1}_{i-1,j} - 4p^{n+1}_{ij} + p^{n+1}_{i,j+1} + p^{n+1}_{i,j-1})/h^2$ and $\nabla_d \cdot \tilde{\mathbf{u}}^n_{ij} = (\tilde{u}^n_{i+\frac{1}{2},j} - \tilde{u}^n_{i-\frac{1}{2},j} + \tilde{v}^n_{i,j+\frac{1}{2}} - \tilde{v}^n_{i,j-\frac{1}{2}})/h$. We solve Eq. (25) by the multigrid method, and using the updated pressure $p^{n+1}$, the divergence-free velocities are obtained

$$u^{n+1}_{i+\frac{1}{2},j} = \tilde{u}^n_{i+\frac{1}{2},j} - \frac{\Delta t}{h}(p^{n+1}_{i+1,j} - p^{n+1}_{ij}), \qquad (26)$$

$$v^{n+1}_{i,j+\frac{1}{2}} = \tilde{v}^n_{i,j+\frac{1}{2}} - \frac{\Delta t}{h}(p^{n+1}_{i,j+1} - p^{n+1}_{ij}). \qquad (27)$$

### 3.2. Dendritic crystal growth on $\Omega_c$

Next, we solve the crystal equation (3) to obtain the updated phase-field function $\phi^n$ on $\Omega_c$. Note that the convection term $\mathbf{u}\cdot\nabla\phi$ is treated by translating and rotating the moving domain $\Omega_{\text{moving}}$. We use the operator splitting scheme [33]:

$$\begin{aligned}
\epsilon^2(\phi^n)\frac{\phi^{n+1,1} - \phi^n}{\Delta t} &= 2\epsilon(\phi^n)\epsilon_x(\phi^n)\phi^n_x + 2\epsilon(\phi^n)\epsilon_y(\phi^n)\phi^n_y \\
&\quad + \left(\frac{16\epsilon_4\epsilon(\phi^n)\phi_x(\phi^2_x\phi^2_y - \phi^4_y)}{|\nabla_d\phi|^4}\right)^n_x \\
&\quad + \left(\frac{16\epsilon_4\epsilon(\phi^n)\phi_y(\phi^2_x\phi^2_y - \phi^4_x)}{|\nabla_d\phi|^4}\right)^n_y, \qquad (28)
\end{aligned}$$

$$\epsilon^2(\phi^n)\frac{\phi^{n+1,2} - \phi^{n+1,1}}{\Delta t} = \epsilon^2(\phi^n)\Delta_d\phi^{n+1,2} - 4\lambda\hat{U}^n F(\phi^{n+1,1}), \qquad (29)$$

where $F(\phi) = 0.25(\phi^2-1)^2$. Because the temperature $U^n$ is defined on $\Omega_f$, we consider the interpolated function $\hat{U}^n$ for $\Omega_c$. $\hat{U}^n_{kl}$ at $\mathbf{s}_{kl} \in \Omega^h_c$ is the bilinearly interpolated value from the temperature $U^n$ at the position $\tilde{\mathbf{s}}_{kl} = \mathbf{X_1} + s^x_k\mathbf{a}/|\mathbf{a}| + s^y_l\mathbf{b}/|\mathbf{b}|$ on $\Omega_f$ (Fig. 5). If $\tilde{\mathbf{s}}_{ij} \notin \Omega_f$, then we define $\hat{U}^n_{ij} = \Delta$ with a dimensionless undercooling $\Delta$.

And then we update $\phi^{n+1}$ by solving the following equation:

$$\phi^{n+1} = \phi^{n+1,2}\Big/\sqrt{e^{-\frac{2\Delta t^*}{\epsilon^2(\phi^{n+1,2})}} + (\phi^{n+1,2})^2\left(1 - e^{-\frac{2\Delta t^*}{\epsilon^2(\phi^{n+1,2})}}\right)}. \qquad (30)$$

Eqs. (25) and (29) are solved by a multigrid method [34]. For more detailed discretizations, please refer to [33].

### 3.3. Translation and rotation of $\Omega_{moving}$

Also, we update the position of the advected crystal on $\Omega_f$ by moving $\Omega_{\text{moving}}$. The magnitudes of its rotatory and parallel translations are derived from the conservations of the linear and angular momentums, respectively. Here, we calculate the velocity $\mathbf{u}^n_c = (u^n_c, v^n_c)$ of the crystal and the rotation angle $\theta^n_c$ of the crystal to represent the motion of the crystal. Using the interpolated phase-field $\tilde{\phi}^n_{ij}$, fluid velocity $\mathbf{u}^n$, and Eq. (7), we can write $\mathbf{u}^n_c$, as

$$\mathbf{u}^n_c = \frac{\sum_{i=1}^{N_x}\sum_{j=1}^{N_y} 0.5\left(1+\tilde{\phi}^n_{ij}\right)\mathbf{u}^n_{ij}h^2}{\sum_{i=1}^{N_x}\sum_{j=1}^{N_y} 0.5\left(1+\tilde{\phi}^n_{ij}\right)h^2}. \qquad (31)$$

Note that the interpolation of $\tilde{\phi}^n$ is described in Section 3.1. And, we estimate the fluid velocity at cell centers as

$$\mathbf{u}^n_{ij} = \left(0.5(u^n_{i+\frac{1}{2},j} + u^n_{i-\frac{1}{2},j}), 0.5(v^n_{i,j+\frac{1}{2}} + v^n_{i,j-\frac{1}{2}})\right). \qquad (32)$$

Next, we consider the angular momentum $\mathbf{L}_c$ of the crystal to calculate the rotation angle $\theta_c$. Let $\omega^n_c$ be an approximation of $\omega_c$ at time $n\Delta t$. From Eq. (9), $\omega^n_c$ is written as

$$\omega^n_c = \frac{\sum_{i=1}^{N_x}\sum_{j=1}^{N_y} 0.5\left(\mathbf{m}^n_c - \mathbf{x}_{ij}\right)\times\mathbf{u}^n_{ij}\left(1+\tilde{\phi}^n_{ij}\right)h^2}{\sum_{i=1}^{N_x}\sum_{j=1}^{N_y}\|\left(\mathbf{m}^n_c - \mathbf{x}_{ij}\right)\|^2 h^2}. \qquad (33)$$

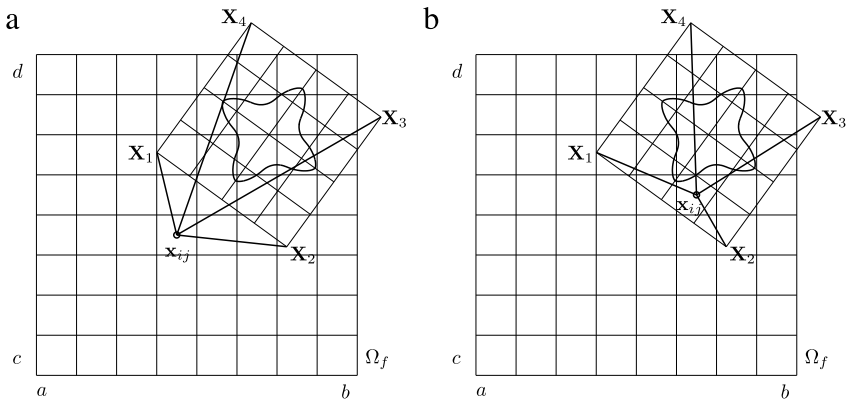


**Fig. 4.** Schematic illustration of (a) $\mathbf{x}_{ij} \notin \Omega_{\text{moving}}$ and (b) $\mathbf{x}_{ij} \in \Omega_{\text{moving}}$.

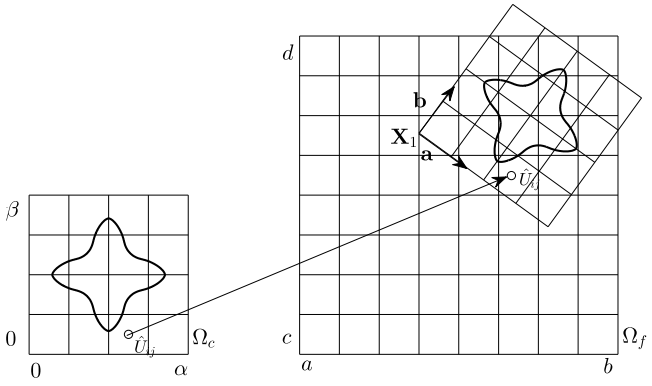


**Fig. 5.** Schematic of the temperature field interpolation.

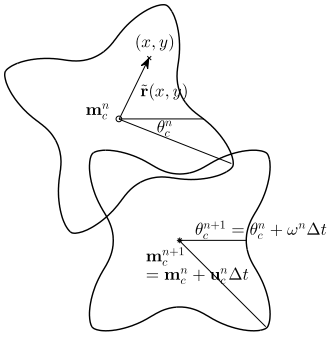


**Fig. 6.** New center position and rotation angle of the crystal domain $\Omega_c$.

Therefore, we can compute the new position and rotation angle of the crystal domain $\Omega_c$ on the fluid domain $\Omega_f$ from Eqs. (31) and (33) (Fig. 6):

$$\mathbf{m}_c^{n+1} = \mathbf{m}_c^n + \mathbf{u}_c^n \Delta t, \tag{34}$$

$$\theta_c^{n+1} = \theta_c^n + \omega_c^n \Delta t. \tag{35}$$

### 3.4. Temperature field on $\Omega_f$

Finally, we solve the temperature field $U$ on the domain $\Omega_f$ with the homogeneous Dirichlet boundary condition using the multigrid method:

$$\frac{U_{ij}^{n+1} - U_{ij}^n}{\Delta t} + (\mathbf{u}^n \cdot \nabla_d U^n)_{ij} = D\Delta_d U_{ij}^{n+1} + \frac{\tilde{\phi}_{ij}^{n+1} - \tilde{\phi}_{ij}^n}{2\Delta t}. \tag{36}$$

Here, we apply the upwind scheme for the advection term:

$$U_{x_{ij}}^n = \begin{cases} \dfrac{U_{ij}^n - U_{i-1,j}^n}{h}, & \text{if } u_{ij}^n > 0, \\ \dfrac{U_{i+1,j}^n - U_{ij}^n}{h}, & \text{otherwise,} \end{cases}$$

$$U_{y_{ij}}^n = \begin{cases} \dfrac{U_{ij}^n - U_{ij-1}^n}{h}, & \text{if } v_{ij}^n > 0, \\ \dfrac{U_{i,j+1}^n - u_{ij}^n}{h}, & \text{otherwise.} \end{cases}$$

Note that the velocity located at a cell center $(u_{ij}^n, v_{ij}^n)$ is defined by using interpolation as $\left(0.5(u_{i+\frac{1}{2},j}^n + u_{i-\frac{1}{2},j}^n), 0.5(v_{i,j+\frac{1}{2}}^n + v_{i,j-\frac{1}{2}}^n)\right)$ as in Section 3.3.

### 3.5. Summary for the implementation

A brief summary of numerical procedures for crystal growth simulation in a cavity flow is as follows: Given the fluid velocity $\mathbf{u}^n$, the phase-field function $\phi^n$, the temperature $U^n$, the crystal location $\mathbf{m}_c^n$, and the crystal rotation $\theta_c^n$, we proceed the following steps:

*Step (1)* Update $\mathbf{u}^{n+1}$ on $\Omega_f$ by Eqs. (11) and (12).
*Step (2)* Update $\phi^{n+1}$ on $\Omega_c$ by Eqs. (28)–(30).
*Step (3)* Update $\mathbf{m}_c^{n+1}$ and $\theta_c^{n+1}$ of $\Omega_{\text{moving}}$ by Eqs. (34) and (35).
*Step (4)* Update $U^{n+1}$ on $\Omega_f$ by Eq. (36).

This completes the description of the process above by which the quantities $\mathbf{u}^{n+1}$, $\phi^{n+1}$, $U^{n+1}$, $\mathbf{m}_c^{n+1}$, and $\theta_c^{n+1}$ are updated.

The fictitious domain model [20] shares a similar idea using the local and global domains to simulate the growth and convection separately; however, there are differences in describing other physical properties. The convection of the crystal is calculated using the correct velocity of the global domain and the momentum equations (or the NS equations) with a permeability term are solved on the local domain in the fictitious domain model. Whereas, we do not solve the NS equations, consider the advection term in $\Omega_c$, and do not implement a permeability term in our model. Instead, the rigid body motion is enforced by calculating the translation and rotation of $\Omega_{\text{moving}}$ and the permeability of the crystal is treated by using a large viscosity ratio. Because of mismatching detail parameters, it is not comparable to compare our method with the results in [20] directly. We would rather perform a numerical simulation in Section 4.2 to compare with the analytical value of a terminal velocity for a particle sedimentation, also suggested in [20].

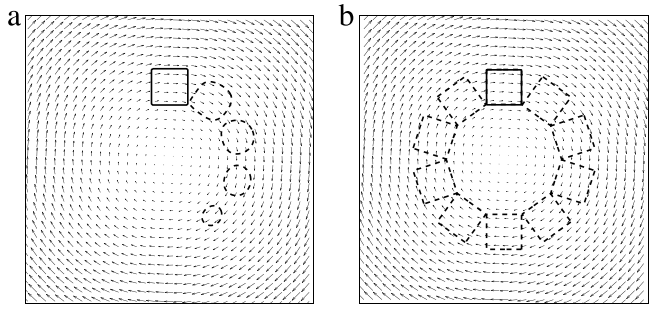


**Fig. 7.** Evolution of the solid under a rotational flow by (a) solving the classical advection equation and (b) applying the proposed overset grid. The solid contour represents the initial configuration, dashed zero-level contours are the configurations at every 400 iterations, and arrows are the underlying velocity field.

**Table 1**
Errors of the numerical angles and the exact value with various mesh grids.

| Mesh | $128^2$ | $256^2$ | $512^2$ |
|---|---|---|---|
| Error | $2.983 \times 10^{-3}$ | $3.260 \times 10^{-4}$ | $6.000 \times 10^{-6}$ |

## 4. Numerical results

In this section, we present examples to numerically demonstrate the efficiency of the proposed methods. The first example compares the result by the proposed translation algorithm with the result by solving the advection equation. Particle sedimentation is computed in the second example to demonstrate the accuracy of our treatment of solid motion. Next, we show temporal evolution of the crystal growth in the two-dimensional cavity flow. We then perform simulations to study the effect of the viscosity, Reynolds number, and temperature.

### 4.1. Translation and rotation of a solid

We first compare the translation and rotation of a solid using the advection equation

$$\frac{\partial \phi}{\partial t} + \mathbf{u} \cdot \nabla \phi = 0 \tag{37}$$

and the proposed algorithm using Eqs. (7) and (10). For simplicity of exposition, we only consider the translation and rotation without solving the crystal growth equation (5). The underlying velocity is a rotational flow $(u, v) = (y/100, -x/100)$ in the domain $\Omega_f = (-50, 50) \times (-50, 50)$, which gives the uniform angular velocity. At the initial state, the square solid whose one side has a length of 12 is located at the center of a quadruply smaller domain $\Omega_c = (0, 50) \times (0, 50)$ and the corresponding moving domain $\Omega_{moving}$ is located at $\mathbf{m}_c^0 = (0, 25)$ in $\Omega_f$. That is,

$$\phi(x, y, 0) = \begin{cases} 1, & \text{if } (x, y) \in \text{ square solid,} \\ -1, & \text{otherwise.} \end{cases}$$

Fig. 7(a) and (b) show the evolution of the solid under the flow with $\Delta t = 0.05\pi$ up to the final time $T = 200\pi$ by solving the classical advection equation and applying the proposed overset grid, respectively. The solid contour represents the initial configuration, dashed zero-level contours are the configurations at every 400 iterations, and arrows are the underlying velocity field. An upwind scheme is applied to solve the classical advection equation. The overset grid method shows the rigid body motion of the solid structure.

Because of the uniform angular velocity $\omega = 0.01$ from the underlying velocity, the initial and final configurations should agree with each other exactly, i.e., the angle is $2\pi$ at the final time $T$. To show the convergence, we perform numerical tests with different mesh sizes for the case as in Fig. 7(b). Table 1 lists the errors of the numerical angles and the exact value at $T$. As the mesh is finer, the angles from the numerical experiments converge to the exact value.

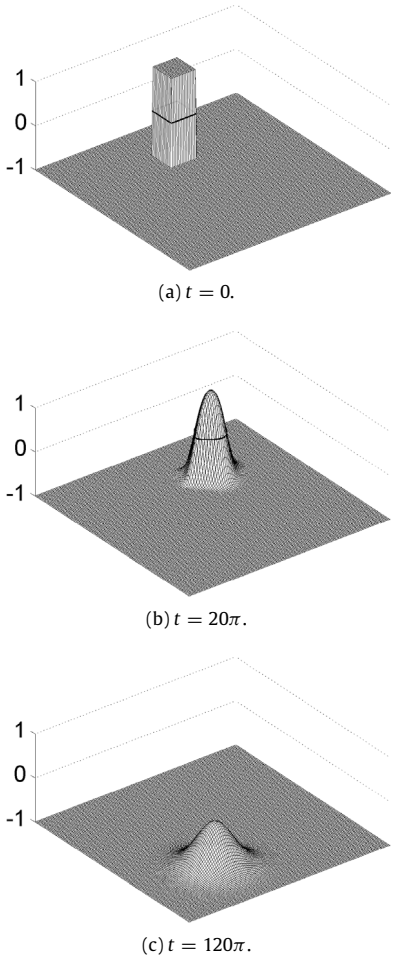


**Fig. 8.** Temporal evolution of $\phi$ with the advection equation (37) and its zero contour (solid line).

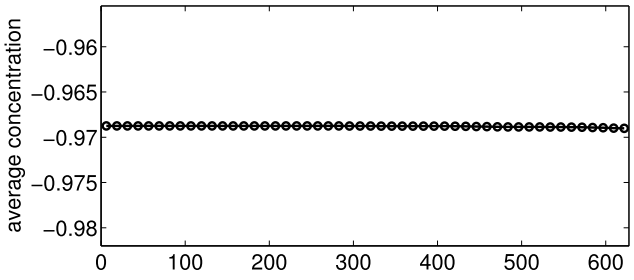


**Fig. 9.** Evolution of average concentration of $\phi$ when solving the advection equation until $t = 200\pi$.

Fig. 8 shows the temporal evolution of $\phi$ with the advection equation (37) and its zero contour. By the numerical diffusion, the zero contour line is shrinking even though its average concentration is preserved as shown in Fig. 9. We could, of course, obtain better results by using other time integrating schemes and smaller time step sizes; however, it is not easy to avoid the numerical diffusion perfectly if the advection equation (37) is used.

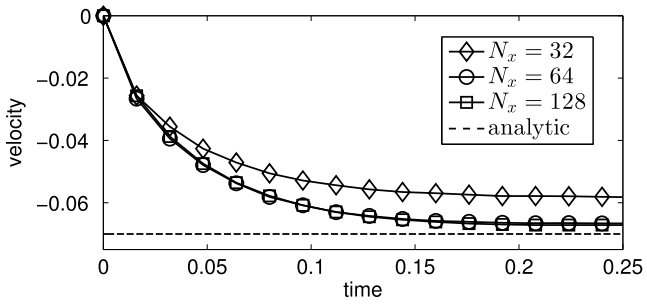


**Fig. 10.** Evolution of the velocity with the different grid numbers.

### 4.2. Particle sedimentation

To demonstrate the accuracy of our treatment of solid motion, we simulate particle sedimentation and compare the results with the analytical value in [35]. Here, the gravitational effect is made by the Boussinesq approximation, which has been widely applied because of its practical simplicity [36–38]. The Navier–Stokes equation with a gravitational force in the Boussinesq approximation can be written as

$$\frac{\partial \mathbf{u}}{\partial t} + \mathbf{u}\cdot\nabla\mathbf{u} = -\frac{1}{\rho^*}\nabla p + \frac{1}{\rho^*}\nabla\cdot[\eta(\phi)(\nabla\mathbf{u} + \nabla\mathbf{u}^T)] + \frac{\rho(\phi)-\rho^*}{\rho^*}\mathbf{g},$$

where $\rho_s$ is the solid density, $\rho_m$ is the density of the ambient fluid, $\rho^* = 0.5(\rho_s + \rho_m)$, $\rho(\phi) = \rho_m + 0.5(\rho_s - \rho_m)(1+\phi)$, and $\mathbf{g} = (0, -g)$ is the gravitational force. The parameters used are as follows: $\Omega_f = [0, 0.04] \times [0, 0.12]$, $\Delta t = 0.2\rho_m h^2 \eta_m/\eta_s$, $h = 0.04/N_x$, $\eta_s = 20$, $\eta_m = 0.5$, $\rho_s = 2000$, $\rho_m = 1000$, $g = 9.8$, and the radius of a solid $r = 0.005$. Under the condition, the analytical terminal velocity is $-0.07$ [35].

Fig. 10 represents the evolution of the velocity with the different grid numbers. The result shows that the terminal velocity converges to the analytical value as $N_x$ becomes bigger. To supplement the solid viscosity effect for a rigid-body motion, we will perform the numerical comparison test for various viscosity ratios in the later section.

### 4.3. Flow effect

We perform numerical experiments for the crystal growth in a two-dimensional cavity flow. To observe the growth of the crystal under the flows, we consider a sufficiently large domain $\Omega_f = [-300, 300] \times [-300, 300]$ to define the fluid and temperature, and we use $\Omega_c = [0, 300] \times [0, 300]$ to define the phase-field representing the crystal. In $\Omega_f$, the time step is restricted to $\Delta t \leq 0.25 Re h^2 \eta_m/\eta_s$ due to the explicit discretization for the diffusion term in Eq. (11). In contrast, in $\Omega_c$, the operator splitting method for solving Eqs. (28)–(29) allows large time step, e.g., $\Delta t \leq 5.5h$ [33]. Thus, we use $\Delta t = \min\left(0.2Re h^2\eta_m/\eta_s, 5.5h\right)$, unless otherwise specified. For the initial state, we take:

$$\phi(x, y, 0) = \tanh\left(\frac{R_0 - \sqrt{x^2+y^2}}{\sqrt{2}}\right) \quad \text{and}$$

$$U(x, y, 0) = \begin{cases} 0 & \text{if } \phi > 0 \\ \Delta & \text{otherwise.} \end{cases}$$

The zero level set ($\phi = 0$) of the initial state represents a circle of radius $R_0 = 6$. From the definition of dimensionless variable $U$, the value of zero corresponds to the melting temperature of the pure material, while the value of $\Delta$ is the initial undercooling. We also use $\lambda = 3.1913$ as in [33,39,40]. The initial center $\mathbf{m}_c^0$ is located at $(0, 120)$ and the initial fluid flow is defined as the steady state solution of the cavity flow $Re = 1$ to reduce the computational time. For other parameters, we set as follows: $h = 600/768$, $\epsilon_4 = 0.05$, $D = 2.0$, $\Delta = -0.3$, $Re = 10$, $\eta_m = 1$, $\eta_s = 25$, and $T = 4272$.

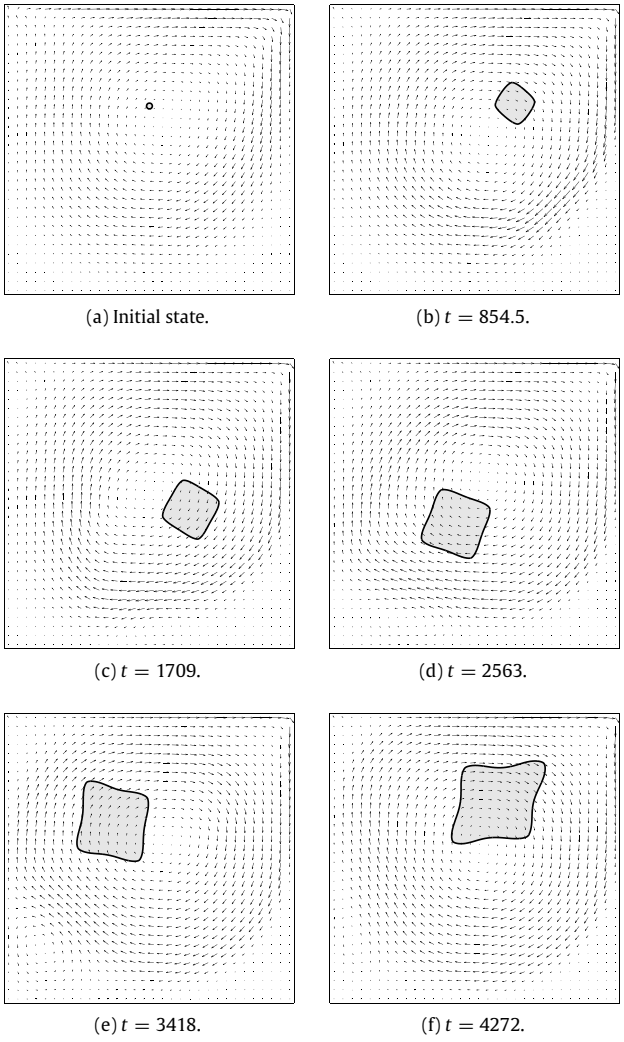

(a) Initial state. (b) $t = 854.5$. (c) $t = 1709$. (d) $t = 2563$. (e) $t = 3418$. (f) $t = 4272$.

**Fig. 11.** Evolutions for the traces of crystal and the flow field.

Fig. 11 shows the temporal evolution of the crystal growth in the cavity flow. The snapshots with the contour of crystal and corresponding fluid vector field are drawn at the specific time. Now, the crystal is not fixed but floats in a liquid, so that the crystal does not grow symmetrically anymore. The flow and crystal affect each other by the viscosity difference, and the crystal follows the fluid flow. The heat distribution is also changed due to the interaction of the flow and crystal, and it makes the non-symmetrical crystal growth.

In addition, Fig. 12 displays the temporal evolutions of crystal growth with and without the cavity flow to show the effect of the flow. Same parameters $\epsilon_4 = 0.05$, $D = 2.0$, and $\Delta = -0.3$ are used in a domain $[0, 300] \times [-150, 150]$ to simulate the crystal growth without the flow. Small difference of growth is observed in the early stage, however, in the case of with the flow, symmetry in growing branches is getting broken and the crystal is growing faster.

**Table 2**
Center of mass $(x_c, y_c)$ and rotational angle $(\theta_c)$ (degree) at the final time $t = 4272$.

| $\eta_s$ | 1.5625 | 3.125 | 6.25 | 12.5 | 25 | 50 | 100 |
|---|---|---|---|---|---|---|---|
| $x_c$ | 346.7044 | 346.3121 | 345.6238 | 344.5754 | 343.2638 | 341.9477 | 340.8277 |
| $y_c$ | 412.2977 | 412.7974 | 413.5656 | 414.5939 | 415.7478 | 416.8293 | 417.7317 |
| $\theta_c$ | 155.1626 | 155.3965 | 155.5990 | 155.7082 | 155.7325 | 155.7314 | 155.7509 |

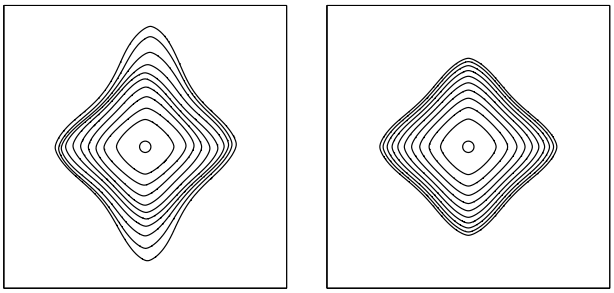

(a) with the flow. (b) without the flow.

**Fig. 12.** Contours of crystal growth (a) with and (b) without the cavity flow. The elapsed time for each contour is 427.2.

### 4.4. Viscosity effect

Here, we show the viscosity effect on a fluid flow. With fixed $\eta_m = 1$, a viscosity ratio is adjusted by $\eta_s$ and the other parameters are the same as the ones in Section 4.3. Table 2 shows the center of mass $(x_c, y_c)$ and the rotational angle $(\theta_c)$ at the final time $t = 4272$.

The flow governed by the Navier–Stokes equation when $Re = 0$ is called the Stokes flow; however, the asymptotic behavior in Stokes flow is fitted well for $Re = 1$, which is small enough to be considered as a limit of the zero Reynolds number [41]. Similarly, we can use a finite value of the viscosity $\eta_s$ to approximate the effect of a solid. Table 2 shows that $\eta_s = 25$ is reasonable in this manner.

We also perform the simulations with higher $Re = 50$ and 100 and compare the effect on the evolution of the crystal growth. Figs. 13(a), (b), and (c) show the interfaces of the crystal and melt with $Re = 10$, 50, and 100 at the final time $t = 4272$, respectively. In each magnified inscribed figure, the results with various viscosity values are shown. The converged contours are the results with $\eta_s = 100$. The results show that the effect of $\eta_s$ becomes weaker as $Re$ becomes larger.

### 4.5. Effect of crystal growth on fluid flow

To show how the crystal growth in $\Omega_c$ may affect the fluid flow in $\Omega_f$, we compare the cavity flow simulations with and without the crystal. Here, the simulation parameters are the same as those of the previous Section 4.3. We exclude $\Omega_c$ and its related parameters for the simulation if there is no crystal.

Fig. 14 shows the overlapped streamlines for each simulation. Here, the solid line is for the result with crystal, while the dotted line is for the result without crystal. At the early stage of the simulations, the streamlines are almost similar for both cases as shown in Fig. 14(a) because the crystal is too small to affect the fluid flow. However, we can easily notice the difference between streamlines when the crystal grows large enough (see Fig. 14(b)). Note that the crystal at $t = 4272$ can be checked in Fig. 11.

### 4.6. Reynolds number effect

Next, we check the Reynolds number effect for the crystal growth in a cavity flow. The used parameters are same as previous simulation in Section 4.3 except for $Re$ and $\Delta t$. For comparison of the Reynolds number effects, we set $Re = 5$ and $Re = 100$. Since the time step restriction depends on $Re$, the corresponding $\Delta t$ is used as 0.02441 and 0.04883 for $Re = 5$ and $Re = 100$, respectively.

Figs. 15(a) and (b) show migration with respect to time and configurations of the crystals at the final time $T$, respectively. A moving distance is little larger when $Re = 100$. Moreover, there is a difference in the growth rates of the crystals with different $Re$ numbers. Generally, absorbing external heat would give rise to growth of crystal. As shown in the figure, migration distance is changed as $Re$ is also changed and it implies that the crystal absorbs more external heat when $Re = 100$ than $Re = 5$. This agrees well with our result for growth of crystal.

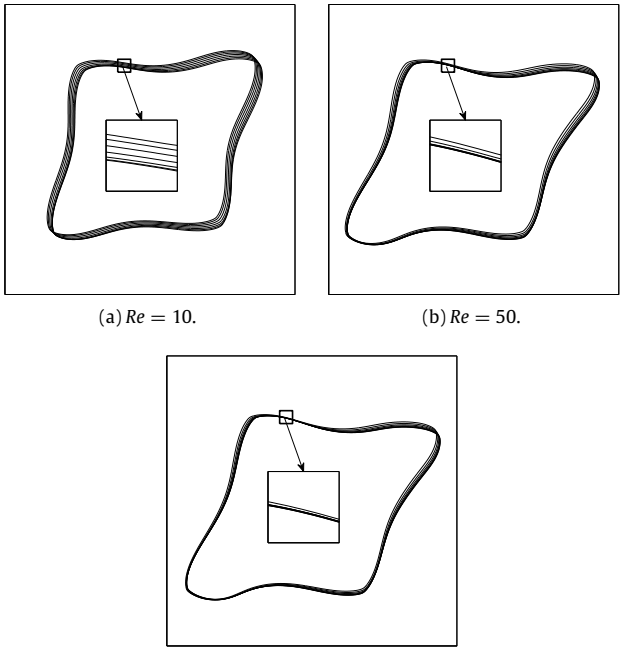

(a) $Re = 10$. (b) $Re = 50$.

(c) $Re = 100$.

**Fig. 13.** Contours of crystal growth with various $\eta_s$ at the final time $t = 4272$.

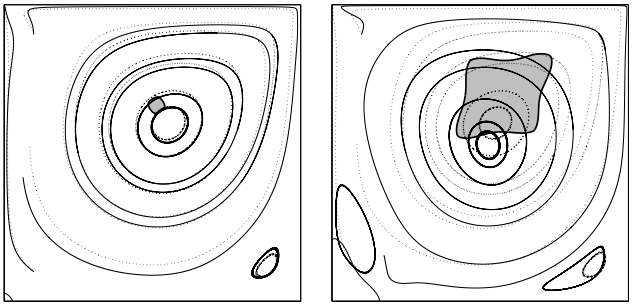

(a) $t = 122.1$. (b) $t = 4272$.

**Fig. 14.** Overlapped streamlines; the solid line is for the result with crystal, while the dotted line is for the result without crystal.

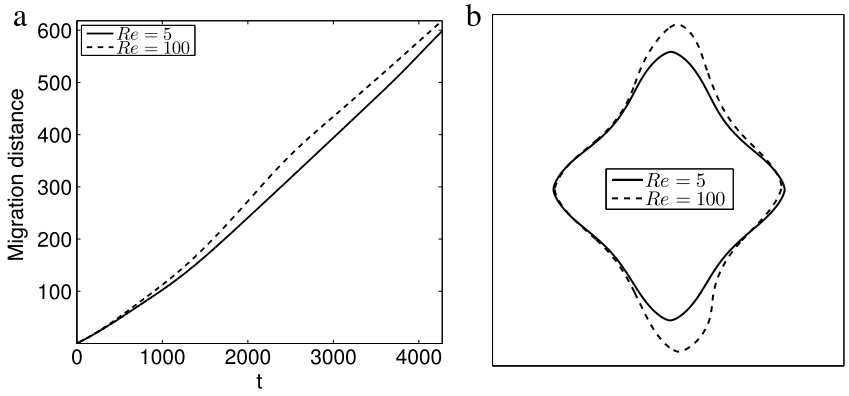


**Fig. 15.** (a) Migration distances with respect to time and (b) contours of the crystals at $T$.

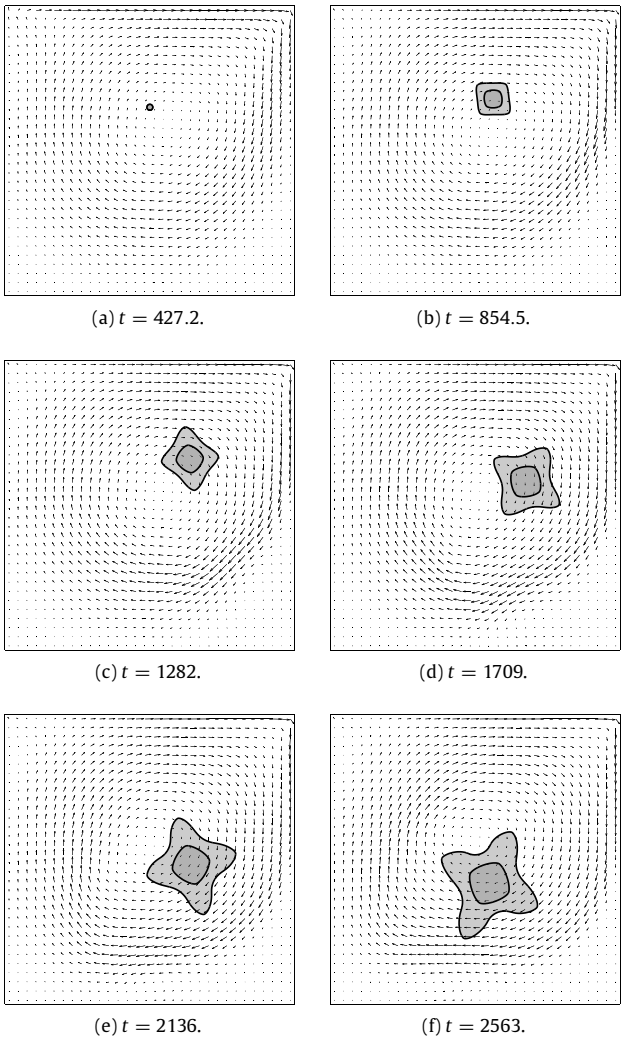

(a) $t = 427.2$. (b) $t = 854.5$. (c) $t = 1282$. (d) $t = 1709$. (e) $t = 2136$. (f) $t = 2563$.

**Fig. 16.** Evolution of the crystal growth under the flow fields with $\Delta = -0.2$ (solid line) and $\Delta = -0.4$ (dotted line).

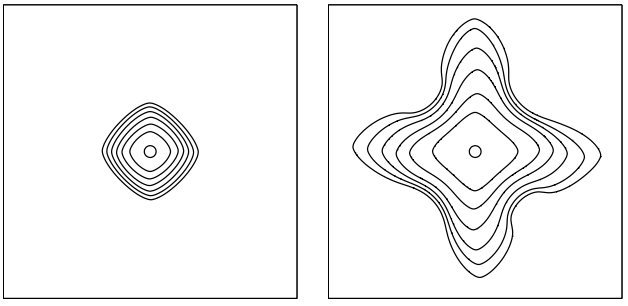

(a) $\Delta = -0.2$. (b) $\Delta = -0.4$.

**Fig. 17.** Contours of crystal growth when (a) $\Delta = -0.2$ and (b) $\Delta = -0.4$. The elapsed time for each contour is 427.2.

### 4.7. Temperature effect

The initial undercooling $\Delta$ is also one of the influential parameter to determine the growth of the crystal. We perform simulations to check the effect of $\Delta$ in the cavity flow. Fig. 16 shows configurations of crystal with $\Delta = -0.2$ and $\Delta = -0.4$ until $t = 2563$. The other parameter settings and initial condition are same as the simulation in 4.3.

Fig. 16 shows the traces of crystal growth under the flow vector fields with $\Delta = -0.2$ (solid line) and $\Delta = -0.4$ (dotted line). Here, the flow vector fields are drawn for better understanding in convection of crystal. As seen in the figures, the crystals with different $\Delta$ have apparently different morphology.

We also display the temporal evolutions of crystal growth when $\Delta = -0.2$ and $\Delta = -0.4$ in Fig. 17 to compare both cases conveniently.

## 5. Discussion

To deal with the case of overgrowth of the crystal in the given initial crystal domain, we increase the crystal domain when the tip position of the crystal is close to the computational domain boundary. We change $\Omega_c = (0, \alpha) \times (0, \beta)$ with $M_x \times M_y$ grid as $\Omega_c = (0, 2\alpha) \times (0, 2\beta)$ with $2M_x \times 2M_y$ grid and define

$$\phi_{kl}^n = \begin{cases} \phi_{k-M_x/2,l-M_y/2}^n, & \text{if } M_x/2+1 \le k \le 3M_x/2 \\ & \text{and } M_y/2+1 \le l \le 3M_y/2, \\ -1, & \text{otherwise.} \end{cases}$$

To valid our extension strategy, we consider a numerical simulation with the same condition as in Fig. 11. Here, we extend the crystal domain if the tip reaches to the boundary layer whose width is $8h$. At the initial stage, the crystal domain size is $\Omega_c = [0, 37.5] \times [0, 37.5]$ with $48 \times 48$ mesh grid.

Fig. 18 shows the evolutions for the traces of crystal and the flow field. The solid box represents the size and the position of $\Omega_c$. Until Fig. 18(c), the result has a good agreement with Fig. 11 which is the result without the proposed extension algorithm. Figs. 18(c),

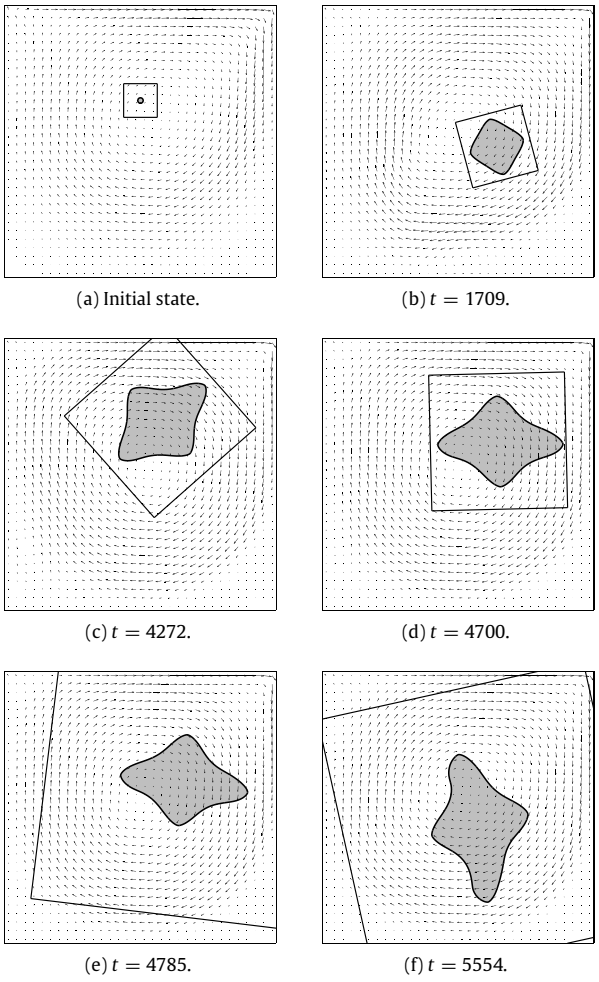

(a) Initial state. (b) $t = 1709$. (c) $t = 4272$. (d) $t = 4700$. (e) $t = 4785$. (f) $t = 5554$.

**Fig. 18.** Evolutions for the traces of crystal and the flow field. The solid box represents the size and the position of $\Omega_c$.

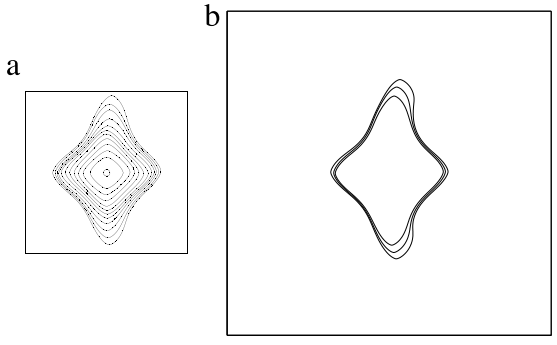


**Fig. 19.** Contours of crystal growth with (a) on the crystal domain smaller than $\Omega_c = [0, 300] \times [0, 300]$ and (b) on the extended crystal domain $\Omega_c = [0, 600] \times [0, 600]$. The elapsed time for each contour is 427.2.

(d), and (e) show the crystal growth after further extension of $\Omega_c$ in Section 4.3. Moreover, Fig. 19 shows the contours of crystal growth with (a) on the crystal domain smaller than $\Omega_c = [0, 300] \times [0, 300]$ and on the extended crystal domains (b) $\Omega_c = [0, 600] \times [0, 600]$. The elapsed time for each contour is 427.2.

In this paper, we only deal with the growth of a single crystal. If the method is further extended to simulate multiple crystals with growth competition, then a natural extensional model is as follows:

$$\frac{\partial \mathbf{u}}{\partial t} + \mathbf{u} \cdot \nabla \mathbf{u} = -\nabla p + \frac{1}{Re} \nabla \cdot [\eta(\psi)(\nabla \mathbf{u} + \nabla \mathbf{u}^T)], \tag{38}$$

$$\nabla \cdot \mathbf{u} = 0, \tag{39}$$

$$\begin{aligned} \epsilon^2(c_i)\left(\frac{\partial c_i}{\partial t} + \mathbf{u} \cdot \nabla c_i\right) &= \nabla \cdot (\epsilon^2(c_i) \nabla c_i) \\ &+ [c_i - 0.5 - \lambda U c_i(1 - c_i)] c_i(1 - c_i) \\ &+ \left(|\nabla c_i|^2 \epsilon(c_i) \frac{\partial \epsilon(c_i)}{\partial c_{ix}}\right)_x \\ &+ \left(|\nabla c_i|^2 \epsilon(c_i) \frac{\partial \epsilon(c_i)}{\partial c_{iy}}\right)_y, \\ &\text{for } i = 1, 2, \ldots, N, \end{aligned} \tag{40}$$

$$\frac{\partial U}{\partial t} + \mathbf{u} \cdot \nabla U = D \Delta U + \frac{\partial \psi}{\partial t}, \tag{41}$$

where $c_i$ is the phase-field of $i$th dendrite that varies from unity in the solid phase to zero in the liquid phase, $N$ is the number of the crystal components, $\psi = \sum_{i=1}^{N} c_i$, and $\eta(\psi) = \eta_s \psi + \eta_m(1 - \psi)$. We suggest that Eq. (40) is solved in an individual crystal domain for each $i$ and expect that growth competition is realized through temperature distribution.

## 6. Conclusion

In this article, we proposed a phase-field model and its computationally efficient numerical method for dendritic growth in a two-dimensional cavity flow. In most of the previous studies, the crystal is fixed in the space and the supercooled melt flows around the crystal, which is hard to be realized in the real world experimental setting. Applying advection to the crystal equation is not simple because we have problems such as deformation of crystal shape and ambiguity of the crystal orientation for the anisotropy. To resolve these difficulties, we presented a phase-field method by using a moving overset grid for the dendritic growth in a cavity flow. Numerical results demonstrated that the proposed method can predict the crystal growth under a flow. Furthermore, we considered the possible strategies to deal with the multiple crystals with growth competition and the single crystal growing larger than the size of the crystal domain in the discussion section. Note that the proposed method heavily relies on the assumption that the solid particle can be well approximated by a very viscous fluid. The solid particle (i.e., the very viscous drop) has two sets of velocities, one is the velocity from fluid equations, and the other is the rigid-body velocity obtained by averaging. In general, these two velocities are different. Besides, as crystal grows, the solid extends to the region which is previously occupied by melt. Therefore, as a future research work, it will be studied to develop a more accurate algorithm for the interaction between the fluid and crystal to the proposed moving overset grid method. Another interesting future research is the extension to three-dimensional space of the two-dimensional methodology.

## Acknowledgments

The corresponding author (J.S. Kim) was supported by the National Research Foundation of Korea (NRF) grant funded by the Korea government (MSIP) (NRF-2014R1A2A2A01003683). The first author (S. Lee) was supported by the National Institute for Mathematical Sciences (NIMS) grant funded by the Korean government (No. A21300000). The author (Y.B. Li) is supported by Natural Science Basic Research Plan in Shaanxi Province of China (2016JQ1024) and by National Natural Science Foundation of China (Nos. 11601416, and 11631012). The author (J. Shin) is supported by Basic Science Research Program through the National Research

Foundation of Korea (NRF), which is funded by the Ministry of Education (2009-0093827). The authors greatly appreciate the reviewers for their constructive comments and suggestions, which have improved the quality of this paper.

## References

[1] M. Cablea, K. Zaidat, A. Gagnoud, A. Nouri, G. Chichignoud, Y. Delannoy, J. Cryst. Growth 417 (1) (2015) 44–50.
[2] S.C. Huang, M.E. Glicksman, Acta Metall. 29 (5) (1981) 701–715.
[3] J.P. Kallungal, A.J. Barduhn, AlChE J. 23 (3) (1977) 294–303.
[4] W.U. Mirihanage, L. Arnberg, R.H. Mathiesen, IOP C. Ser. Mater. Sci. Engrg. 33 (1) (2012) 012033.
[5] N. Shevchenko, O. Roshchupkina, O. Sokolova, S. Eckert, J. Cryst. Growth 417 (2015) 1–8.
[6] R. Tönhardt, G. Amberg, J. Cryst. Growth 213 (2000) 161–187.
[7] R. Rojas, T. Tokaki, M. Ohno, J. Comput. Phys. 298 (2015) 29–40.
[8] C. Beckermann, H.-J. Diepers, I. Steinbach, A. Karma, X. Tong, J. Comput. Phys. 154 (1999) 468–496.
[9] J.M. Debierre, A. Karma, F. Celestini, R. Guérin, Phys. Rev. E 68 (2003) 041604.
[10] J.-H. Jeong, J.A. Dantzig, N. Goldenfeld, Metall. Mater. Trans. A 34A (2003) 459–466.
[11] J.-H. Jeong, N. Goldenfeld, J.A. Dantzig, Phys. Rev. E 64 (2001) 041602.
[12] X. Tong, C. Beckermann, A. Karma, Q. Li, Phys. Rev. E 63 (2001) 061601.
[13] A. Abdollahi, I. Arias, Arch Comput. Methods Eng. 22 (2) (2015) 153–181.
[14] L. Chen, J. Chen, R.A. Lebensohn, Y.Z. Ji, T.W. Heo, S. Bhattacharyya, L.Q. Chen, Comput. Methods Appl. Mech. Engrg. 285 (2015) 829–848.
[15] Y. Ma, M. Plapp, J. Cryst. Growth 385 (2014) 140–147.
[16] G. Tierra, F. Guillén-Gonzalez, Arch. Comput. Methods Eng. 22 (2) (2015) 269–289.
[17] C.C. Chen, Y.L. Tsai, C.W. Lan, Int. J. Heat Mass Transfer 52 (2009) 1158–1166.
[18] C.C. Chen, C.W. Lan, J. Cryst. Growth 312 (8) (2010) 1437–1442.
[19] M. Zhu, D. Sun, S. Pan, Q. Zhang, D. Raabe, Model. Simul. Sci. Eng. 22 (3) (2014) 034006.
[20] M. Do-Quang, G. Amberg, J. Comput. Phys. 227 (2008) 1772–1789.
[21] S. Karagadde, A. Bhattacharya, G. Tomar, P. Dutta, J. Comput. Phys. 231 (2012) 3987–4000.
[22] E. Casoni, A. Jérusalem, C. Samaniego, B. Eguzkitza, P. Lafortune, D.D. Tjahjanto, X. Sáez, G. Houzeaux, M. Vázquez, Arch. Comput. Methods Eng. 22 (4) (2015) 557–576.
[23] Z. Guo, S.M. Xiong, Comput. Phys. Comm. 190 (2015) 89–97.
[24] B. Jelinek, M. Eshraghi, S. Felicelli, J.F. Peters, Comput. Phys. Comm. 185 (3) (2014) 939–947.
[25] P.G. Tennyson, G.M. Karthik, G. Phanikumar, Comput. Phys. Comm. 186 (2015) 48–64.
[26] S. Lee, Ph.D. thesis, Korea University, 2016.
[27] Y. Choi, D. Jeong, S. Lee, J. Kim, J. KSIAM 9 (2) (2015) 103–201.
[28] J. Kim, Int J. Comput. Methods 2 (2) (2005) 201–212.
[29] J.A. Dantzig, Internat. J. Numer. Methods Engrg. 28 (8) (1989) 1769–1785.
[30] G.B. Arfken, H.J. Weber, Mathematical Methods for Physicisists, sixth ed., Elsevier, Oxford, 2005.
[31] A.J. Chorin, 22 (1968) 745–762.
[32] Y. Li, A. Yun, D. Lee, J. Shin, D. Jeong, J. Kim, Comput. Methods Appl. Mech. Engrg. 257 (2013) 36–46.
[33] Y. Li, H.G. Lee, J. Kim, J. Cryst. Growth 321 (1) (2011) 176–182.
[34] U. Trottenberg, C. Oosterlee, A. Schüller, Multigrid, Academic Press, London, 2001.
[35] F. Gibou, C. Min, Efficient symmetric positive definite second-order accurate monolothic solver for fluid/solid interactions, J. Comput. Phys. 231 (2012) 3246–3263.
[36] D. Jacqmin, J. Comput. Phys. 155 (1999) 96–127.
[37] J. Kim, J.S. Lowengrub, Interfaces Free Bound. 7 (2005) 435–466.
[38] C. Liu, J. Shen, Physica D 179 (2003) 211–228.
[39] Y. Li, J. Kim, Int. J. Heat Mass Transfer 55 (2012) 7929–7932.
[40] J. Rosam, P.K. Jimack, A. Mullis, J. Comput. Phys. 225 (2007) 1271–1287.
[41] D.B. Khismatullin, Y. Renardy, V. Cristini, Phys. Fluids 15 (5) (2003) 1351–1354.